Asian Journal of Chemistry; Vol. 38, No. 2 (2026), 334-342
ASIAN JOURNAL OF CHEMISTRY
https://doi.org/10.14233/ajchem.2026.34942

Rutin-Mediated Synthesis of Zr-Mg@N-rGO Nanocomposites with Potent Antioxidant and Antimicrobial Activities

S. NIVETHA[1], J. ROSALINE VIMALA[1,*], A. DEVADHARSHINI AMALA[1] and A. ANITHA IMMACULATE[2]

[1]PG and Research Department of Chemistry, Holy Cross College (Autonomous), Affiliated to Bharathidasan University, Tiruchirappalli-620002, India
[2]Emmet A. Denis College of Natural Sciences, Cuttington University, Suakoko, Bong County, Liberia

*Corresponding author: E-mail: rosalinevimala@hcctrichy.ac.in

Received: 23 September 2025 *Accepted*: 15 December 2025 *Published online*: 31 January 2026 AJC-22251

In present study, a novel Zr-Mg@N-doped reduced graphene oxide (N-rGO) nanocomposite was synthesized using a green, sustainable approach. Rutin, a natural polyphenolic flavonoid, was employed as a reducing and stabilizing agent, enabling the eco-friendly fabrication of the nanocomposite without the use of harsh chemicals. The synthesized material was thoroughly characterized using multiple techniques. UV-visible spectroscopy confirmed nanoparticle formation and optical properties; FT-IR analysis revealed the presence of functional groups associated with rutin and metal-oxygen bonds; XRD patterns indicated the crystalline nature of ZrO_2 and MgO phases embedded within the rGO matrix; SEM and EDAX analyses confirmed the morphological features and elemental composition, while DLS and zeta potential measurements indicated good colloidal stability and moderate mono dispersity. The nanocomposite exhibited significant bacterial (*Actinomyces israelii*, *Proteus vulgaris*) and fungal (*Candida albicans*, *Trichoderma*) pathogens with increasing inhibition zones observed at higher concentrations. Antioxidant potential was evaluated *via* DPPH, H_2O_2 and NO assays, where the nanocomposite demonstrated dose-dependent free radical scavenging activity, attributed to the presence of rutin and synergistic metal-oxide interaction. Overall, the synthesized Zr-Mg@N-rGO nanocomposite offers a multifunctional platform with potential applications in biomedical, environmental and optoelectronic fields.

Keywords: Doped reduced graphene oxide, Green synthesis, Rutin, Biological activity, Multifunctional properties.

INTRODUCTION

The swift progress in nanotechnology has significantly advanced the design of multifunctional materials tailored to meet essential demands in targeted drug delivery and therapeutic applications. Among these, bimetallic nanoparticles supported on carbon-based materials such as nitrogen-doped reduced graphene oxide (N-rGO) are emerging as highly effective drug carriers [1]. N-rGO provides a high surface area, tunable electronic properties and several functional groups, which enable the uniform dispersion and stabilization of bimetallic nanoparticles within its matrix [2,3].

Integrating zirconium and magnesium into the N-rGO framework further enhances the performance of nanocarriers [4,5]. Zirconium offers exceptional biocompatibility, structural stability and corrosion resistance, crucial for maintaining carrier integrity during systemic circulation [6-9]. Magnesium imparts additional bioactivity and facilitates cellular interactions, promoting improved drug retention and targeted delivery efficiency [10]. Together, these metals synergize within the graphene matrix to create a stable and biologically responsive platform capable of enhancing drug loading and release profiles [11].

The functionalization of graphene composite with rutin, a natural flavonoid known for its potent antioxidant and anticancer properties, further augments the therapeutic potential of the nanocarrier [12]. Rutin contributes not only its intrinsic bioactivity but also improves the nanocomposite's stability, biocompatibility and solubility, addressing challenges typically faced by bioactive compounds in clinical translation [13]. The novel rutin mediated Zr-Mg@N-rGO nanocomposite combines the unique properties of each component to facilitate efficient drug encapsulation, protection and controlled release, making it a promising candidate for next-generation targeted drug delivery systems [14-16]. This study systematically explores its synthesis, physico-chemical characterization and evaluates

its drug-carrying capabilities alongside *in vitro* therapeutic efficacy, highlighting its relevance for advanced biomedical applications.

EXPERIMENTAL

Graphite powder (as precursor for graphene oxide synthesis), zirconium oxychloride octahydrate ($ZrOCl_2 \cdot 8H_2O$) and magnesium acetate ($Mg(CH_3COO)_2$) served as source for zirconium and magnesium doping, respectively. Sodium hydroxide and ammonium hydroxide (as nitrogen source), along with conc. suphuric acid and potassium permanganate, were utilized in the modified Hummers' method for graphene oxide preparation. Rutin was used as a reference antioxidant in relevant assays. Deionized water was employed throughout the experiments. The analytical grade chemicals and solvents were procured from reputable suppliers and used without further modification unless otherwise specified.

Synthesis of nitrogen-doped reduced graphene oxide (N-rGO): Graphene oxide (GO) was synthesized from graphite powder *via* a modified Hummers' method [17], involving oxidation with conc. sulphuric acid and potassium permanganate, followed by thorough washing and exfoliation. For nitrogen doping, the obtained GO was dispersed in deionized water and mixed with ammonium hydroxide as a nitrogen source. The mixture was transferred to a Teflon-lined autoclave and subjected to hydrothermal treatment at 180 ºC for 12 h, resulting in simultaneous reduction and nitrogen doping of GO. The product (N-rGO) was filtered, washed with water and dried at 60 ºC. Nitrogen doping was confirmed by FT-IR and EDAX elemental analysis.

Synthesis of metallic oxide (Zr/MgO_2) nanoparticles: Rutin (0.05 g) dissolved in 50 mL of ethanol was added to $ZrOCl_2 \cdot 8H_2O/Mg(CH_3COO)_2 \cdot 4H_2O$ (0.2 M, 10 mL) solution under constant stirring at room temperature. A 1 M NaOH was then added gradually to adjust the pH to 10, initiating the co-precipitation of metallic hydroxide. The mixture was stirred for 6 h, during which rutin acted as a reducing and capping agent controlling particle growth. The precipitate was centrifuged, washed with water and ethanol, dried overnight at 80 ºC and calcined at 400 ºC for 3 h to obtain crystalline ZrO_2/MgO nanoparticles [18,19].

Synthesis of Zr-Mg@N-rGO nanocomposite: A weighed amount of N-rGO (0.2 g) was ultrasonicated in 100 mL of deionized water for 30 min to form a stable suspension [20]. Separately, 0.1 M $Mg(CH_3COO)_2 \cdot 4H_2O$ and 0.1 M $ZrOCl_2 \cdot 8H_2O$ solutions were prepared in deionized water and added to the N-rGO suspension under stirring for uniform metal ion dispersion. Rutin dissolved in ethanol was added dropwise to the mixture. Co-precipitation was initiated by slowly adding 1 M NaOH until the pH reached 9-11, causing zirconium and magnesium hydroxides to precipitate onto the N-rGO sheets along with rutin incorporation. The mixture was stirred for 4 h at room temperature or mildly heated (60-80 ºC) to enhance crystallinity. The precipitate was collected by centrifugation, washed with water and ethanol and dried under vacuum at 50 ºC [21].

Characterization: SEM (CARL ZEISS EVO 18) showed uniform particle distribution and prevented agglomeration, while XRD confirmed well-defined crystalline phases. FTIR (Perkin-Elmer Spectrum 2, 4000-400 cm^{-1}) revealed the functional groups and EDX verified elemental composition and nitrogen doping of graphene. The UV-visible spectroscopy was performed using a Perkin-Elmer Lambda 35 spectrophotometer over the wavelength range of 190-1100 nm to confirm the presence of rutin and N-rGO. Dynamic light scattering (DLS) measurements were carried out using a Micromeritics Nano Plus instrument to determine the hydrodynamic particle size and assess colloidal stability, while zeta potential analysis confirmed the high dispersion stability of the nanoparticles.

Biological assessments: The biological activities of the synthesized nanocomposites were evaluated through antimicrobial and antioxidant assays. Antibacterial and antifungal properties were assessed using standard *in vitro* diffusion-based methods. For antibacterial testing, agar well and disk diffusion techniques [22] were applied on nutrient agar plates inoculated with bacterial strains such as *Proteus vulgaris* and *Actinomyces israelii*. Clear inhibition zones after incubation at varying sample concentrations provided a quantitative measure of antibacterial potency. Antifungal activity was similarly tested on potato-dextrose agar plates seeded with *Candida albicans* and *Trichoderma*, with inhibition zones indicating antifungal effectiveness [23]. Gentamicin and amphotericin B served as positive controls for bacteria and fungi, respectively. Antioxidant potential was determined *via* colorimetric assays [24] measuring the nanocomposites' ability to scavenge free radicals and mitigate oxidative stress.

RESULTS AND DISCUSSION

FT-IR spectrum of N-rGO: The FT-IR spectrum of N-rGO (Fig. 1) reveals several characteristic absorption bands that confirm the presence of key functional groups and successful doping [25]. The broad absorption around 3444 cm^{-1} is attributed to O–H and N–H stretching vibrations, indicating the presence of hydroxyl groups and possible nitrogen containing functionalities introduced during doping [18]. The peak near 2070 cm^{-1} is typically assigned to C–H stretching vibrations, which may arise from residual hydrocarbon chains or edge groups. The band at 1633 cm^{-1} is associated with C–N stretching, providing evidence for successful nitrogen doping into the graphene lattice. Finally, the peak at 713 cm^{-1} can be attributed to C–O stretching vibrations, indicating that some oxygen-containing groups remain after reduction. Overall, this FT-IR spectrum confirms the partial reduction of GO, the introduction of nitrogen functionalities and the retention of some oxygenated groups, all of which are consistent with the expected structure of N-rGO [26].

EDX spectrum: The EDX spectrum for the N-rGO sample (Fig. 2) reveals the elemental composition of the material. The spectrum is dominated by a very strong peak for carbon (C), which is expected due to the graphene-based nature of the sample. A significant oxygen (O) peak is also present, indicating the presence of residual oxygen-containing functional groups, which are common in reduced graphene oxide even after reduction and doping. A nitrogen signal is discernible in the spectrum; however, its intensity is relatively low, as nitrogen is typically present in minor concentrations and may partially

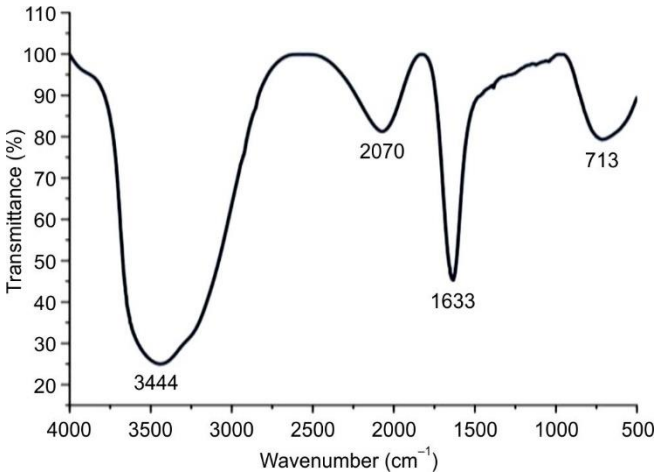

Fig. 1. FT-IR spectrum of N-rGO

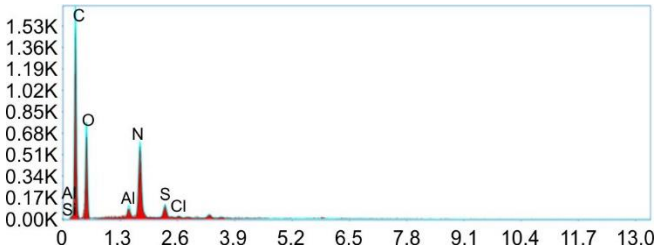

Fig. 2. EDX spectrum for N-rGO

overlap with or appear weaker than, the dominant carbon and oxygen peaks. The absence of strong peaks for metals or other dopants suggests that the sample is primarily composed of carbon, nitrogen and oxygen, with minor contributions from other elements. Overall, this EDX spectrum confirms that the N-rGO sample is rich in carbon, contains a significant amount of oxygen and may have trace elements from the synthesis process or environment. The elemental composition supports the successful synthesis of N-doped reduced graphene oxide, with the expected dominance of carbon and the presence of oxygen and possible dopant or impurity elements [27].

UV-visible spectra: Fig. 3 shows the UV-Vis absorption spectra of ZrO_2, MgO and Zr-Mg@N-rGO nanocomposite. The synthesized Zr-Mg@N-rGO nanocomposite exhibits the characteristic peaks at 205 nm, 234 nm and 291 nm, reflecting the combined electronic transitions of nitrogen-doped reduced graphene oxide and metal oxides, respectively. The prominent peak at 205 nm is attributed to π–π* transitions within the conjugated graphene framework, confirming successful integration of N-rGO [28]. Additional absorption features at 234 nm and 291 nm indicate the presence and electronic interactions of Zr and Mg oxide species within the composite. Compared to discrete Mg and Zr nanoparticles, which show absorption maxima at 206 nm and 203 nm, respectively, the spectral shifts of nanocomposite and enhanced absorbance intensities evidence strong interfacial coupling and synergistic effects between metal oxides and the graphene substrate, implicating improved optoelectronic properties and functionality [29].

FT-IR spectra: The FTIR spectra of the ZrO_2, MgO and Zr-Mg@N-rGO nanocomposite are presented in Fig. 4. The Zr-Mg@N-rGO spectrum features a broad peak at 3436 cm^{-1}, corresponding to hydroxyl (–OH) group vibrations and

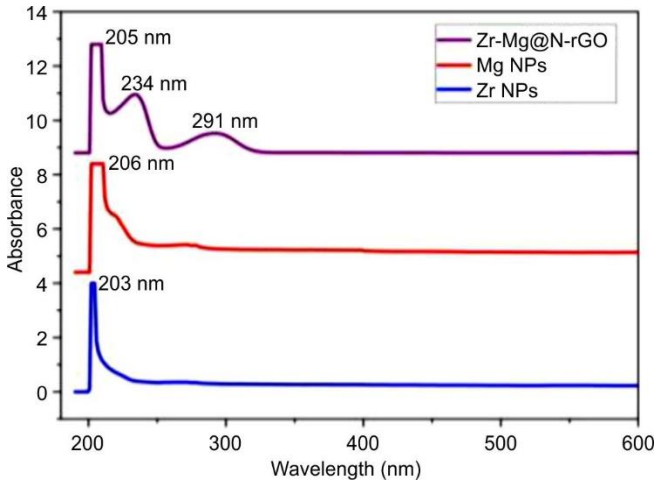

Fig. 3. UV-vis spectra of ZrO_2, MgO and Zr-Mg@N-rGO nanocomposite

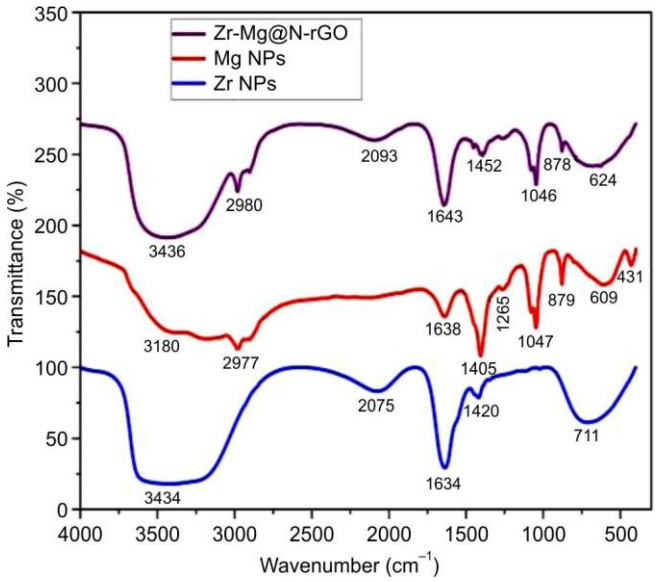

Fig. 4. FTIR spectra of ZrO_2, MgO and Zr-Mg@N-rGO nanocomposite

adsorbed moisture, indicating surface functionalization and hydrogen bonding. Peaks at 2980 cm^{-1} arise from aliphatic C–H stretching are likely associated with the residual organic groups from N-rGO. The absorption at 2093 cm^{-1} indicates the presence of C≡C or C≡N groups, confirming effective nitrogen doping within the graphene structure. Prominent bands at 1643 and 1452 cm^{-1} correspond to aromatic C=C stretching, demonstrating retention of the graphitic framework after synthesis. The peaks at 1046 and 878 cm^{-1} are attributed to C–O stretching and bending, respectively, highlighting the oxygen-containing functionalities that help nanoparticle anchoring. The metal–oxygen vibrations are evident in the fingerprint region with bands at 624 and 609 cm^{-1} representing Zr–O and Mg–O bonds, respectively [30].

Morphology: Fig. 5 shows high-resolution SEM images ZrO_2, MgO and Zr-Mg@N-rGO nanocomposite depicting the morphological characteristics. Zirconium nanoparticles exhibit irregular and angular morphologies with evident agglomeration and rough surface texture, indicative of high surface energy and particle-particle interactions [31]. MgO nanoparticles present a predominantly spherical and densely

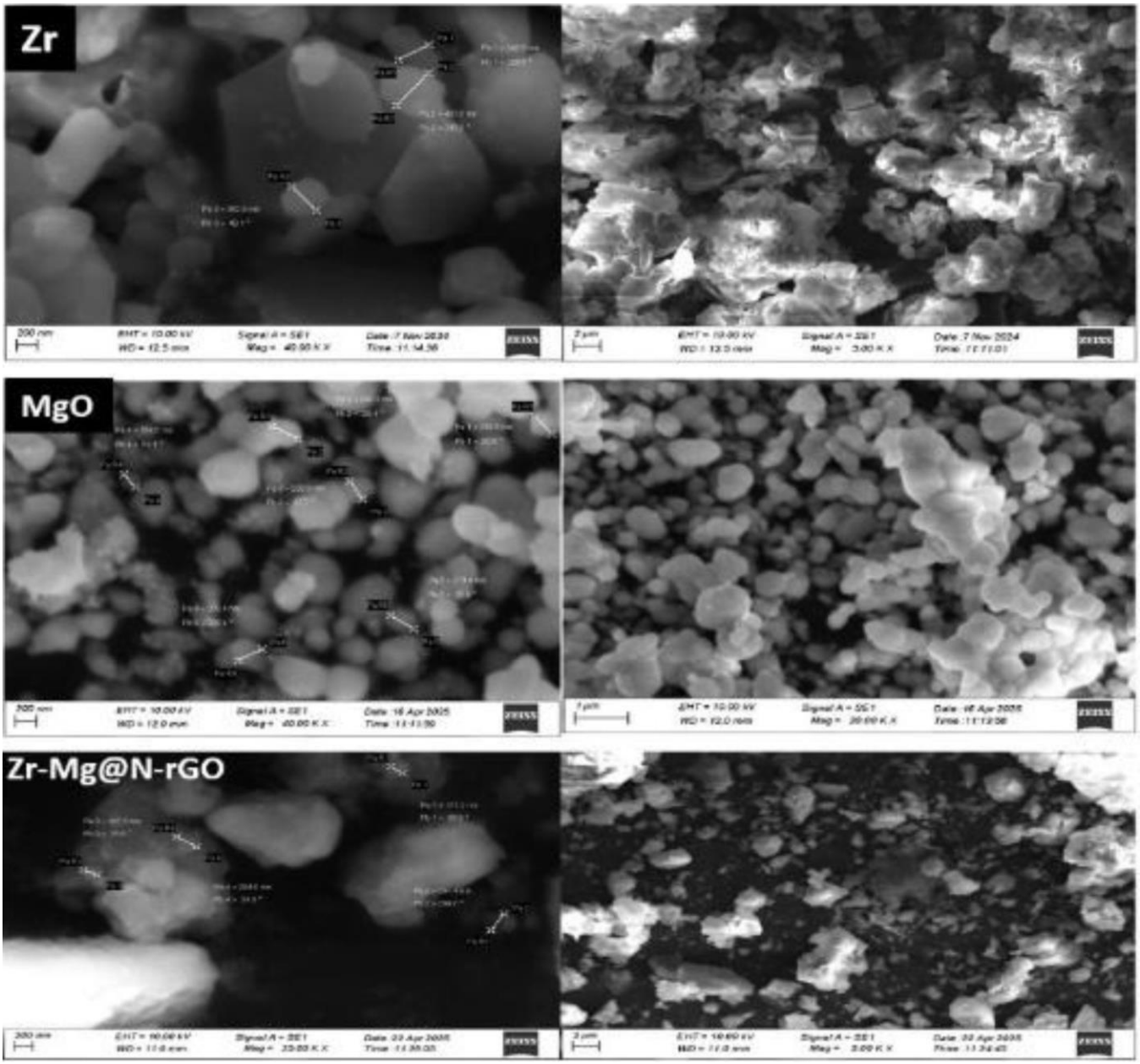

Fig. 5. SEM images of ZrO_2, MgO and Zr-Mg@N-rGO nanocomposite

packed arrangement with relatively uniform particle size distribution, reflecting controlled nucleation and growth conditions during synthesis. The Zr-Mg@N-rGO nanocomposite reveals a heterogeneous morphology characterized by uniform dispersion of Zr and MgO nanoparticles anchored onto the wrinkled, sheet-like architecture of N-rGO. The graphene substrate effectively inhibits nanoparticle aggregation by providing a high surface area platform, promoting enhanced metal oxide distribution and interfacial interactions. These morphological characteristics are intrinsically linked to the nanocomposite's enhanced physico-chemical stability and provide a structural basis for its multifunctional performance, particularly in catalytic and drug-delivery applications [32].

X-ray diffraction: Fig. 6 displays the XRD patterns of ZrO_2, MgO and the Zr-Mg@N-rGO nanocomposite, revealing the characteristic crystalline phases of the individual components and confirming their successful structural integration during synthesis. The ZrO_2 nanoparticles exhibit multiple sharp diffraction peaks, confirming well-defined crystallinity aligned with monoclinic or tetragonal zirconia reference profiles. The MgO nanoparticles display intense reflections, notably around $2\theta \approx 36^{\circ}$ and 42°, characteristic of the cubic phase and indicative of phase purity and high crystallinity [33]. For the Zr-Mg@N-rGO nanocomposite, the pattern is dominated by highly intense, sharp peaks attributable to both ZrO_2 and MgO, along with signals associated with the reduced graphene oxide matrix, demonstrating successful incorporation and homogenous dispersion of the metal oxides within the carbon scaffold. Enhanced peak broadening in the composite further suggests nanometric particle size and interfacial interactions, collectively signifying a well-engineered hybrid structure with preserved and synergistic crystalline properties [34].

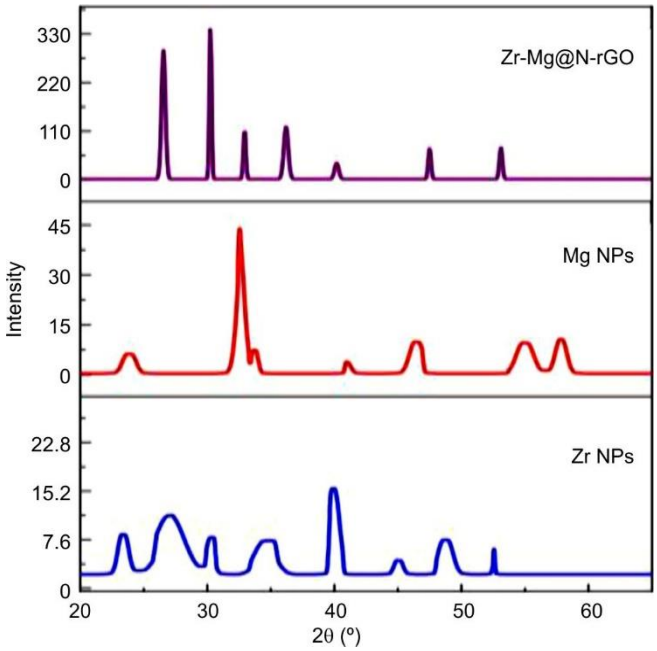

Fig. 6. XRD spectra of ZrO_2, MgO and Zr-Mg@N-rGO nanocomposite

Energy dispersive X-ray analysis: The EDX spectra (Fig. 7) for ZrO_2, MgO and Zr-Mg@N-rGO nanocomposite confirm the elemental composition and purity of each sample. The ZrO_2 spectrum displays dominant peaks for zirconium (Zr) and oxygen (O), affirming the presence of ZrO_2, with only minimal traces of chlorine likely from precursor residues [35]. The MgO spectrum reveals strong magnesium (Mg) and oxygen (O) peaks, alongside minor sodium (Na) and silicon (Si) signals, indicating high purity and successful formation of MgO nanoparticles. The Zr-Mg@N-rGO nanocomposite features prominent peaks for both Zr and Mg, along with substantial oxygen content and the appearance of a carbon (C) signal, which is characteristic of the Zr-Mg@N-rGO matrix. The combined and intense Zr and Mg peaks in the composite spectrum substantiate the effective integration of both metal oxides in the graphene framework. These findings collectively validate the successful synthesis, compositional uniformity and purity of the individual nanoparticles and the ternary nanocomposite [36]. Overall, these EDX results validate the elemental makeup and efficient integration in the designed nanomaterials.

Dynamic light scattering (DLS): The DLS data and autocorrelation function (ACF) plots provide insight into the particle size distribution and colloidal stability of ZrO_2, MgO nanoparticles and the Zr-Mg@N-rGO nanocomposite [37]. For ZrO_2 nanoparticles, the intensity distribution histogram shows a relatively narrow size distribution centered around approximately 65 nm (Fig. 8a), indicating a uniform particle population. The corresponding ACF decay curve exhibits a gradual decline, suggesting moderate colloidal stability with limited aggregation over the measured timescale. The MgO nanoparticles show a broader intensity distribution, with particle sizes spanning a wider range approximately from 30 to 100 nm, indicating polydispersity and a less uniform size population. The ACF plots (Fig. 8b) similarly reveal consistent decay over time, reflecting moderately good dispersion but with potential for slight particle aggregation or heterogeneity [38].

In case of the Zr-Mg@N-rGO nanocomposite, the size distribution histogram is broader and more asymmetric, with particle diameters extending roughly from 30 to 120 nm. This wider distribution likely reflects the presence of metal oxide nanoparticles combined with graphene sheets, contributing to a complex hybrid structure. The ACF curve shows a steady decay similar to the individual nanoparticles, implying reasonable colloidal stability of the composite suspension, despite the increased polydispersity [39]. Overall, the DLS and ACF results demonstrate that all three samples produce nanoscale particles with sufficient colloidal stability, with the Zr-Mg@N-rGO nanocomposite exhibiting the most complex size profile due to its hybrid nature. This data supports the successful synthesis of well-dispersed nanoparticles suitable for further biomedical or catalytic applications [40].

Zeta potential: Fig. 9 shows the zeta potential distribution plot of the Zr-Mg@N-rGO nanocomposite shows a sharp peak around +25 mV, indicating that the particles possess a moderate positive surface charge. Zeta potential is a key indicator of colloidal stability; values above +25 mV or below –25 mV generally represents good electrostatic repulsion between particles, minimizing aggregation. The positive charge may be attributed to surface functional groups introduced by Zr, Mg oxides or rutin capping, which help stabilize the nanoparticles in aqueous media. The presence of rutin, a polyphenolic flavonoid, can also contribute to stability *via* both electrostatic and steric hindrance. Thus, the observed zeta potential suggests that the nanocomposite has good colloidal stability, making it suitable for biological, environmental and catalytic applications where dispersion and surface interaction are critical [41].

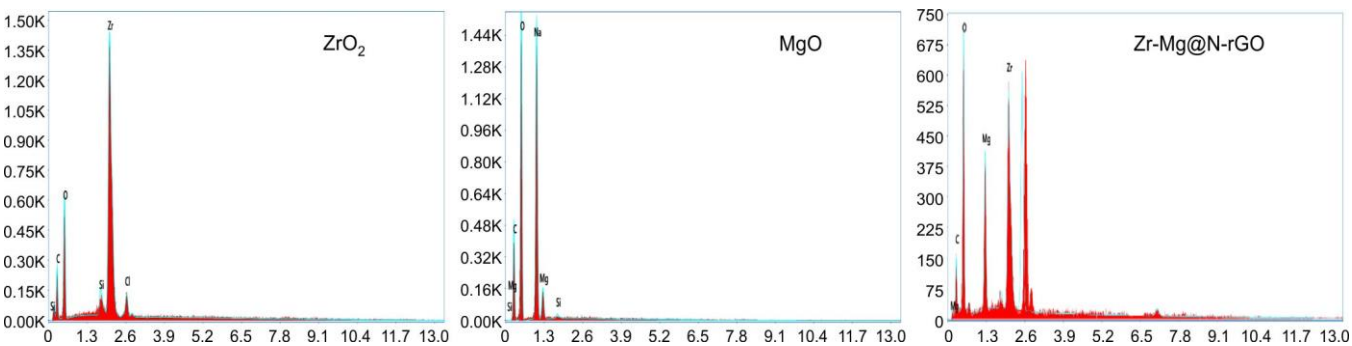

Fig. 7. EDAX spectra of ZrO_2, MgO and Zr-Mg@N-rGO nanocomposite

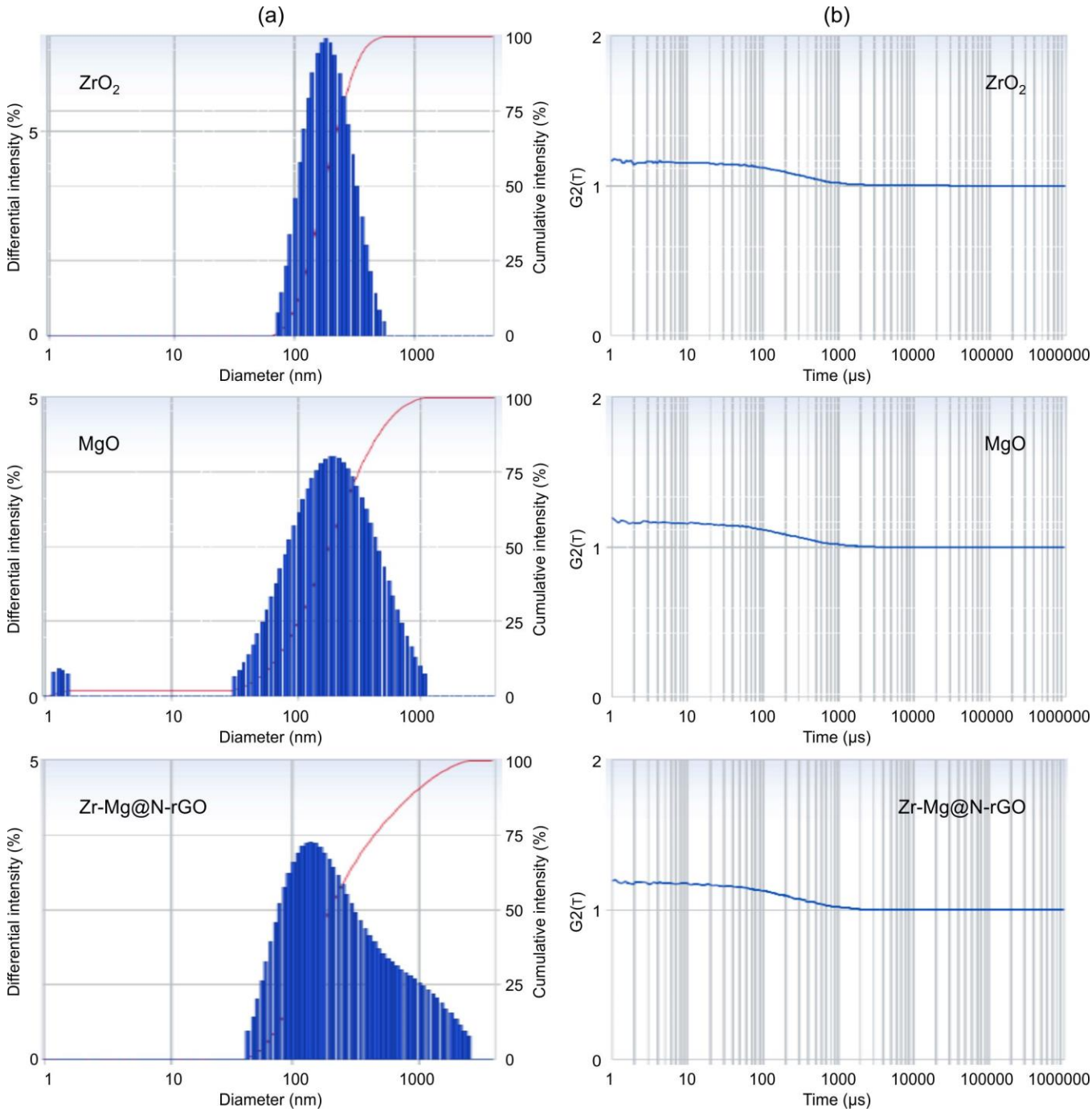

Fig. 8. DLS (a) and ACF (b) plots of ZrO_2, MgO and Zr-Mg@N-rGO nanocomposite

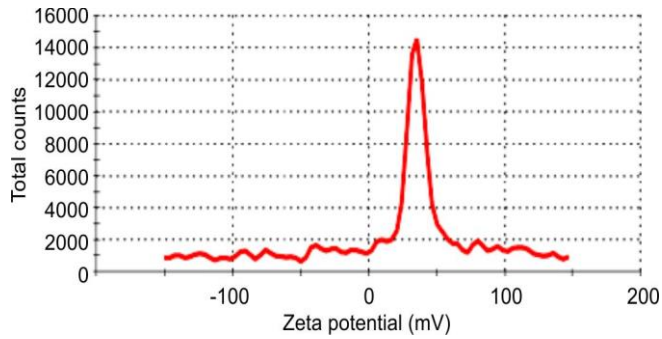

Fig. 9. Zeta potential curve of Zr-Mg@N-rGO nanocomposite

Antimicrobial activity: The antimicrobial activity of the Zr-Mg@N-rGO was clearly evidenced by the formation of substantial zones of inhibition against both selected bacterial (*Actinomyces israelii*, *Proteus vulgaris*) and fungal (*Candida albicans*, *Trichoderma*) pathogens when tested at varying concentrations of 500 μg/mL and 250 μg/mL (Fig. 10). At these higher concentrations, the mean diameters of inhibition zones ranged from 14.85 ± 0.21 mm to 15.6 ± 0.14 mm across all tested organisms, indicating a significant suppression of microbial growth. In contrast, no inhibition zones were observed at lower concentrations of 100 μg/mL and 50 μg/mL, highlighting the presence of a threshold effect where the antimicrobial

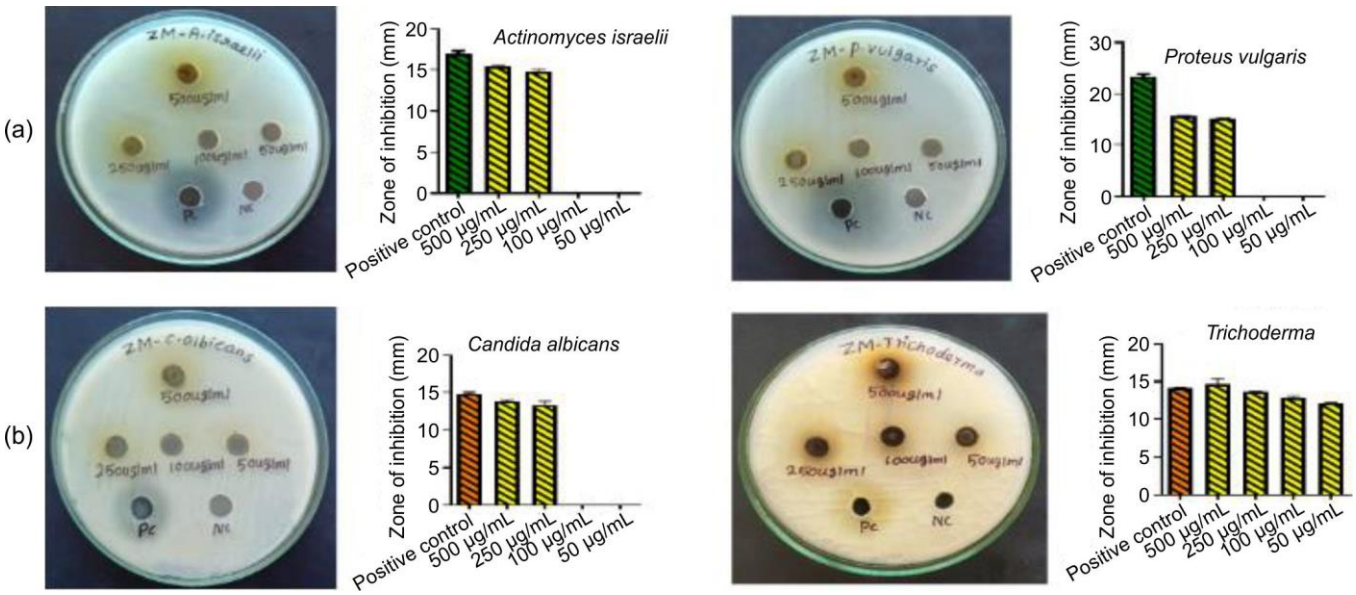

Fig. 10. (a) Antibacterial activity and (b) antifungal activity results of Zr-Mg@N-rGO nanocomposite

efficacy of the Zr-Mg@N-rGO nanocomposite is only substantial above a certain dose. However, the positive control consistently produced larger zones of inhibition (16.95 ± 0.35 mm to 23.35 ± 0.49 mm), as expected for standard antibiotics or antifungal agents (Table-1). These comparative results indicate that although the synthesized nanocomposite does not fully match the potency of standard reference drugs, it approaches their effectiveness at higher concentrations [42,43]. The observed dose-dependence of the inhibition zones further emphasizes that the antimicrobial effect of the nanocomposite increases with concentration and is reproducible among both bacterial and fungal strains.

DPPH radical scavenging assay: The antioxidant capacity of the prepared Zr-Mg@N-rGO nanocomposite was evaluated by the DPPH radical scavenging assay, measured as a decrease in absorbance at 517 nm. The sample exhibited a concentration-dependent inhibition of DPPH radicals, with higher concentrations resulting in greater scavenging activity. The percent inhibition ranged from approximately 5.9% at 10 µg/mL to 48.4% at 500 µg/mL, indicating moderate free radical neutralization potential compared to the positive control, ascorbic acid (Fig. 11), which showed over 96% inhibition [40]. The IC_{50} value of 36.27 µg/mL reflects the antioxidant potency and shows a relatively strong radical scavenging ability, although lower than the standard antioxidant ascorbic acid. The fit of the curve was statistically robust, with a Hill slope of -1.97 and an R^2 of 0.955, indicating a high degree of reliability in the IC_{50} estimate [45]. Thus, the results demonstrate

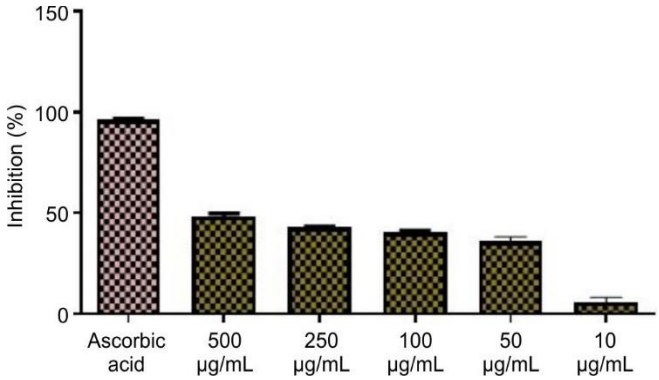

Fig. 11. DPPH radical scavenging results of Zr-Mg@N-rGO

that the Zr-Mg@N-rGO nanocomposite possesses significant antioxidant activity, as supported by its capacity to effectively reduce stable free radicals in the DPPH assay [45].

Hydrogen peroxide scavenging assay: The results display in Fig. 12, a concentration-dependent increase in antioxidant activity of the Zr-Mg@N-rGO nanocomposite. At each tested concentration, the percentage of inhibition reflects the effectiveness of the sample in neutralizing hydrogen peroxide. The ability of the sample to neutralize H_2O_2 was assessed based on the reduction in absorbance at 230 nm following incubation with varying concentrations of the nanocomposite. The control (phosphate buffer containing H_2O_2) exhibited a mean optical density of 0.352 and was used as baseline. The nanocomposite demonstrated a dose-dependent H_2O_2 scavenging activity, with

TABLE-1
ANTIMICROBIAL EFFICACY AND ZONE OF INHIBITION DATA OF Zr-Mg@N-rGO NANOCOMPOSITE

	Test organism	Zone of inhibition (mm), Mean ± SD		
		500 µg/mL	250 µg/mL	Positive control
Bacterial	*Actinomyces israelii*	15.35 ± 0.21	14.85 ± 0.21	16.95 ± 0.35
	Proteus vulgaris	15.6 ± 0.14	15.1 ± 0.14	23.35 ± 0.41
Fungal	*Candida albicans*	15.35 ± 0.21	14.85 ± 0.21	16.95 ± 0.35
	Trichoderma	15.6 ± 0.14	15.1 ± 0.14	23.35 ± 0.49

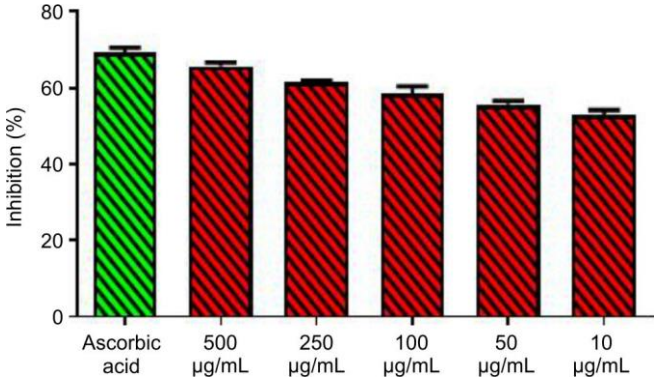

Fig. 12. H_2O_2 activity scavenging results of Zr-Mg@N-rGO

inhibition increasing from 53.13% at 10 µg/mL to 65.72% at 500 µg/mL. The calculated IC_{50} value was 123.0 µg/mL, indicating moderate antioxidant efficacy. Ascorbic acid, as positive control, showed the highest inhibition (69.32%), confirming the assay sensitivity. The concentration-dependent response substantiates the reproducibility and reliability of the antioxidant activity [46].

Nitric oxide radical scavenging assay: Nitric oxide scavenging activity was evaluated by measuring the reduction in absorbance at 540 nm following reaction with the Griess reagent. The control exhibited a mean OD of 1.2583. The Zr-Mg@N-rGO nanocomposite showed a clear dose-dependent inhibition of nitric oxide generation (Fig. 13), evidenced by progressively decreasing absorbance with increasing concentration [47]. An IC_{50} value of 68.74 µg/mL was obtained, indicating a relatively strong NO scavenging capacity. This result underscores the effective antioxidant potential of synthesized nanocomposite and suggests possible anti-inflammatory activity, consistent with reported effects of plant-derived antioxidants in alleviating nitrosative stress [48-50].

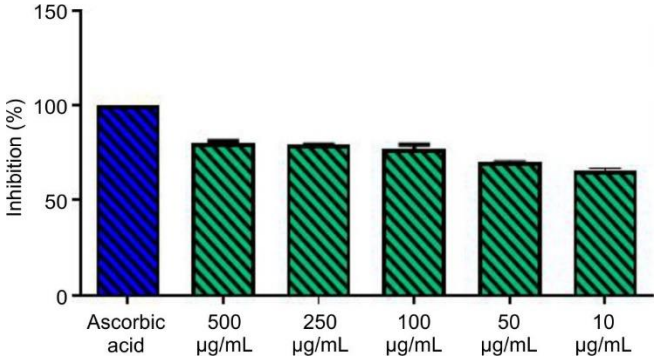

Fig. 13. Nitric oxide activity results of Zr-Mg@N-rGO

Conclusion

The present study successfully demonstrated the synthesis of zirconium oxide and magnesium oxide nanoparticles and their hybrid nanocomposite with nitrogen-doped reduced graphene oxide. The integration of metal oxide nanoparticles within the graphene framework resulted in a structurally stable material with improved dispersion and synergistic properties. The nanocomposite exhibited notable antimicrobial and antioxidant activities, highlighting its multifunctional nature. These findings indicate that the Zr-Mg@N-rGO nanocomposite is a promising candidate for advanced biomedical and environmental applications, and the study provides a useful strategy for designing graphene-based hybrid nanomaterials with enhanced functional performance.

ACKNOWLEDGEMENTS

The authors thank the Department of Science and Technology (DST), Government of India, for providing the support through Fund for Improvement of S&T Infrastructure in Universities and Higher Educational Institutions (FIST) program (Grant No. SR/FIST/College-/2020/943).

CONFLICT OF INTEREST

The authors declare that there is no conflict of interests regarding the publication of this article.

DECLARATION OF AI-ASSISTED TECHNOLOGIES

During the preparation of this manuscript, the authors used an AI-assisted tool(s) to improve the language. The authors reviewed and edited the content and take full responsibility for the published work.

REFERENCES

1. J.A.A. Abdullah, H. Ali Mohammed, C. Salmi, Z. Alqarni, S. Eddine Laouini, A. Guerrero and A. Romero, *Bioorg. Chem.*, **153**, 107828 (2024); https://doi.org/10.1016/j.bioorg.2024.107828
2. S.R.A. Kumar, D.V. Mary, G.A.S. Josephine and M.A.R. Ahamed, *Hybrid Adv.*, **5**, 100168 (2024); https://doi.org/10.1016/j.hybadv.2024.100168
3. H.-C. Youn, S.-M. Bak, M.-S. Kim, C. Jaye, D. A. Fischer, C.-W. Lee, X.-Q. Yang, K.C. Roh and K.-B. Kim, *ChemSusChem*, **8**, 1875 (2015); https://doi.org/10.1002/cssc.201500122
4. S. Sagadevan, Z.Z. Chowdhury, M.E. Hoque and J. Podder, *Mater. Res. Express*, **4**, 115031 (2017); https://doi.org/10.1088/2053-1591/aa9a8c
5. F. Liu, Z. Wang, X. Du, S. Li and W. Du, *Materials*, **16**, 2303 (2023); https://doi.org/10.3390/ma16062303
6. M. Ghafori-Gorab, A. Kashtiaray, M. Karimi, H.A.M. Aliabadi, F. Bakhtiyar, F.D. Ghadikolaei, M. Mohajeri and A. Maleki, *Chem. Eng. J.*, **505**, 159464 (2025); https://doi.org/10.1016/j.cej.2025.159464
7. G. Srinivasan, A. Manickam, S. Sivakumar, J. Murugan, S. Elangomannan and S. Mohan, *J. Mater. Sci.: Mater. Eng.*, **20**, 76 (2025); https://doi.org/10.1186/s40712-025-00294-9
8. V. Cepeda, M. Ródenas-Munar, S. García, C. Bouzas and J.A. Tur, *Antioxidants*, **14**, 740 (2025); https://doi.org/10.3390/antiox14060740
9. G. Fatima, A. Dzupina, H.B. Alhmadi, A. Magomedova, Z. Siddiqui, A. Mehdi and N. Hadi, *Cureus*, **16**, e71392 (2024); https://doi.org/10.7759/cureus.71392
10. S. Qamar, N. Ramzan and W. Aleem, *Synth. Met.*, **307**, 117697 (2024); https://doi.org/10.1016/j.synthmet.2024.117697
11. R. Darabi, F.E.D. Alown, A. Aygun, Q. Gu, F. Gulbagca, E.E. Altuner, H. Seckin, I. Meydan, G. Kaymak, F. Sen and H. Karimi-Maleh, *Int. J. Hydrogen Energy*, **48**, 21270 (2023); https://doi.org/10.1016/j.ijhydene.2022.12.072
12. P. Salehpour and A. Abri, *Colloids Surf. B: Biointerfaces*, **220**, 112903 (2022); https://doi.org/10.1016/j.colsurfb.2022.112903
13. Y. Peng, M. Liao, X. Ma, H. Deng, F. Gao, R. Dai and L. Lu, *Int. J. Electrochem. Sci.*, **14**, 4946 (2019); https://doi.org/10.20964/2019.06.28
14. H.R. Tantawy, A.A. Nada, A. Baraka and M.A. Elsayed, *Appl. Surf. Sci. Adv.*, **3**, 100056 (2021); https://doi.org/10.1016/j.apsadv.2021.100056

15. A.P. Ayanwale, B.L. Estrada-Capetillo and S.Y. Reyes-López, *Inorg. Chem. Commun.*, **134**, 108954 (2021); https://doi.org/10.1016/j.inoche.2021.108954
16. Z.M. Mohammedsaleh and F.M. Saleh, *J. Drug Deliv. Sci. Technol.*, **83**, 104397 (2023); https://doi.org/10.1016/j.jddst.2023.104397
17. R. Sanjinés, M.D. Abad, C. Vâju, R. Smajda, M. Mionić and A. Magrez, *Surf. Coat. Technol.*, **206**, 727 (2011); https://doi.org/10.1016/j.surfcoat.2011.01.025
18. B. Murtaza, A. Naseer, M. Imran, N. Shah, A.A. Al-Kahtani, Z.A. ALOthman, M. Shahid, J. Iqbal, G. Abbas, N. Natasha and M. Amjad, *Environ. Geochem. Health*, **45**, 9003 (2023); https://doi.org/10.1007/s10653-023-01630-8
19. C.E. Zou, J. Zhong, S. Li, H. Wang, J. Wang, B. Yan and Y. Du, *J. Electroanal. Chem.*, **805**, 110 (2017); https://doi.org/10.1016/j.jelechem.2017.10.020
20. M.I. Alghonaim, S.A. Alsalamah, A.M. Mohammad and T.M. Abdelghany, *Biomass Convers. Biorefin.*, **15**, 6767 (2025); https://doi.org/10.1007/s13399-024-05451-2
21. M. Ashrafizadeh, H. Saebfar, M.H. Gholami, K. Hushmandi, A. Zabolian, P. Bikarannejad, M. Hashemi, S. Daneshi, S. Mirzaei, E. Sharifi, A.P. Kumar, H. Khan, H.H.S. Hossein, M. Vosough, N. Rabiee, V.K. Thakur, P. Makvandi, Y.K. Mishra, F.R. Tay, Y. Wang, A. Zarrabi, G. Orive and E. Mostafavi, *Expert Opin. Drug Deliv.*, **19**, 355 (2022); https://doi.org/10.1080/17425247.2022.2041598
22. M. Balouiri, M. Sadiki and S.K. Ibnsouda, *J. Pharm. Anal.*, **6**, 71 (2016); https://doi.org/10.1016/j.jpha.2015.11.005
23. Y. Liu, G. Tortora, M.E. Ryan, H.-M. Lee and L.M. Golub, *Antimicrob. Agents Chemother.*, **46**, 1455 (2002); https://doi.org/10.1128/AAC.46.5.1455-1461.2002
24. J. Flieger, N. Żuk, E. Grabias-Blicharz, P. Puźniak and W. Flieger, *Antioxidants*, **14**, n1506 (2025); https://doi.org/10.3390/antiox14121506
25. N.G. Dlamini, A.K. Basson and V.S.R. Pullabhotla, *Appl. Nano*, **4**, 1 (2023); https://doi.org/10.3390/applnano4010001
26. P. Srinoi, Y.T. Chen, V. Vittur, M.D. Marquez and T.R. Lee, *Appl. Sci.*, **8**, 1106 (2018); https://doi.org/10.3390/app8071106
27. M.E. Khan, M.M. Khan and M.H. Cho, *New J. Chem.*, **39**, 8121 (2015); https://doi.org/10.1039/C5NJ01320H
28. A. Khanmohammadi, V. Rashidi and S. Sadighian, *Biointerface Res. Appl. Chem.*, **13**, 383 (2023); https://doi.org/10.33263/BRIAC134.383392
29. D. Medina-Cruz, B. Saleh, A. Vernet-Crua, A. Nieto-Argüello, D. Lomelí-Marroquín, L.Y. Vélez-Escamilla, J.L. Cholula-Díaz, J.M. García-Martín and T. Webster, in eds.: B. Li, T. Moriarty, T. Webster and M. Xing, Bimetallic Nanoparticles for Biomedical Applications: A Review, In: Racing for the Surface. Springer, Cham., pp. 397-434 (2020).
30. Y. Qiu, Z. Wang, A.C. Owens, I. Kulaots, Y. Chen, A.B. Kane and R.H. Hurt, *Nanoscale*, **6**, 11744 (2014); https://doi.org/10.1039/C4NR03275F
31. S. Bera, M. Ghosh, M. Pal, N. Das, S. Saha, S.K. Dutta and S. Jana, *RSC Adv.*, **4**, 37479 (2014); https://doi.org/10.1039/C4RA06243D
32. F. Fu, Z. Cheng and J. Lu, *RSC Adv.*, **5**, 85395 (2015); https://doi.org/10.1039/C5RA13067K
33. C. Wang, B. Li, W. Niu, S. Hong, B. Saif, S. Wang, C. Dong and S. Shuang, *RSC Adv.*, **5**, 89299 (2015); https://doi.org/10.1039/C5RA13082D
34. H. Ghadimi, B. Nasiri-Tabrizi, P.M. Nia, W.J. Basirun, R.M. Tehrani and F. Lorestani, *RSC Adv.*, **5**, 99555 (2015); https://doi.org/10.1039/C5RA18109G
35. G. Darabdhara, M.A. Amin, G.A.M. Mersal, E.M. Ahmed, M.R. Das, M.B. Zakaria, V. Malgras, S.M. Alshehri, Y. Yamauchi, S. Szunerits and R. Boukherroub, *J. Mater. Chem. A Mater. Energy Sustain.*, **3**, 20254 (2015); https://doi.org/10.1039/C5TA05730B
36. A.S. Siddiqui, M.A. Ahmad, M.H. Nawaz, A. Hayat and M. Nasir, *Catalysts*, **12**, 1105 (2022); https://doi.org/10.3390/catal12101105
37. A. Ghamkhari, S. Abbaspour-Ravasjani, M. Talebi, H. Hamishehkar and M.R. Hamblin, *Int. J. Biol. Macromol.*, **169**, 521 (2021); https://doi.org/10.1016/j.ijbiomac.2020.12.084
38. S. Pattnaik, K. Swain and Z. Lin, *J. Mater. Chem. B Mater. Biol. Med.*, **4**, 7813 (2016); https://doi.org/10.1039/C6TB02086K
39. C.M. Santos, J. Mangadlao, F. Ahmed, A. Leon, R.C. Advincula and D.F. Rodrigues, *Nanotechnology*, **23**, 395101 (2012); https://doi.org/10.1088/0957-4484/23/39/395101
40. A. Ahmad, A.S. Qureshi, L. Li, J. Bao, X. Jia, Y. Xu and X. Guo, *Colloids Surf. B Biointerfaces*, **143**, 490 (2016); https://doi.org/10.1016/j.colsurfb.2016.03.065
41. R.M. Fathy and A.Y. Mahfouz, *J. Nanostructure Chem.*, **11**, 301 (2021); https://doi.org/10.1007/s40097-020-00369-3
42. I. Kritika and I. Roy, *Mater. Adv.*, **3**, 7425 (2022); https://doi.org/10.1039/D2MA00444E
43. A. Abedini, M. Rostami, H.R. Banafshe, M. Rahimi-Nasrabadi, A. SobhaniNasab and M.R. Ganjali, *Front Chem.*, **10**, 893793 (2022); https://doi.org/10.3389/fchem.2022.893793
44. N. Matinise, N. Mayedwa, K. Kaviyarasu, Z.Y. Nuru, I.G. Madiba, N. Mongwaketsi, X. Fuku and M. Maaza, *Mater. Today Proc.*, **36**, 401 (2021); https://doi.org/10.1016/j.matpr.2020.04.743
45. Z. Hao, M. Wang, L. Cheng, M. Si, Z. Feng and Z. Feng, *Front. Bioeng. Biotechnol.*, **11**, 1337543 (2024); https://doi.org/10.3389/fbioe.2023.1337543
46. P. Ranga Reddy, K. Varaprasad, N. Narayana Reddy, K. Mohana Raju and N.S. Reddy, *J. Appl. Polym. Sci.*, **125**, 1357 (2012); https://doi.org/10.1002/app.35192
47. M. Das, U. Goswami, R. Kandimalla, S. Kalita, S.S. Ghosh and A. Chattopadhyay, *ACS Appl. Bio Mater.*, **2**, 5434 (2019); https://doi.org/10.1021/acsabm.9b00870
48. F. Ali, S.B. Khan, T. Kamal, Y. Anwar, K.A. Alamry and A.M. Asiri, *Chemosphere*, **188**, 588 (2017); https://doi.org/10.1016/j.chemosphere.2017.08.118
49. T. Doolotkeldieva, S. Bobusheva, Z. Zhasnakunov and A. Satybaldiev, *J. Nanomater.*, **2022**, 1190280 (2022); https://doi.org/10.1155/2022/1190280
50. C.G. Ugwuja, O.O. Adelowo, A. Ogunlaja, M.O. Omorogie, O.D. Olukanni, O.O. Ikhimiukor, I. Iermak, G.A. Kolawole, C. Guenter, A. Taubert, O. Bodede, R. Moodley, N.M. Inada, A.S.S. De Camargo and E.I. Unuabonah, *ACS Appl. Mater. Interfaces*, **11**, 25483 (2019); https://doi.org/10.1021/acsami.9b01212